Multi-Scale Coherent Magnetic Field from Atomic Medium to L1544 Molecular Core

Tao-Chung Ching (chingtaochung@gmail.com)
CAS Key Laboratory of FAST, NAOC, Chinese Academy of Sciences https://orcid.org/0000-0001-8516-2532

Di Li
National Astronomical Observatories, Chinese Academy of Sciences https://orcid.org/0000-0003-3010-7661

Carl Heiles
University of California, Berkeley

Zhi-Yun Li
University of Virginia

Lei Qian
National Astronomical Observatories, Chinese Academy of Sciences https://orcid.org/0000-0003-0597-0957

Youling Yue
National Astronomical Observatories, Chinese Academy of Sciences https://orcid.org/0000-0003-4415-2148

Jing Tang
National Astronomical Observatories, Chinese Academy of Sciences

Sihan Jiao
National Astronomical Observatories, Chinese Academy of Sciences

Physical Sciences - Article

Keywords: magnetic fields, Zeeman measurements

Posted Date: March 24th, 2021

DOI: https://doi.org/10.21203/rs.3.rs-343684/v1

Multi-Scale Coherent Magnetic Field from Atomic Medium to L1544 Molecular Core

T.-C. Ching[1] *, D. Li[1,2]†, C. Heiles[3], Z.-Y. Li[4], L. Qian[1], Y. L. Yue[1], J. Tang[1], S. H. Jiao[1,2]

[1]*CAS Key Laboratory of FAST, NAOC, Chinese Academy of Sciences, Beijing 100101, China*

[2]*University of Chinese Academy of Sciences, Beijing 100049, China*

[3]*University of California, Berkeley, CA 94720, USA*

[4]*Astronomy Department, University of Virginia, Charlottesville, VA 22904, USA*

Magnetic fields play an important role in the evolution of interstellar medium and star formation [1,2]. As the only direct tracer of interstellar field strength, credible Zeeman measurements remain sparse due to rather limited number of spectral lines with discernible Zeeman effect, particularly for cold, molecular gas[3]. Here we report the detection of a magnetic field of 3.8 ± 0.3 μG through a new tracer, the HI narrow self-absorption (HINSA)[4,5], toward the prestellar core L1544 of the Taurus molecular cloud using the Five-hundred-meter Aperture Spherical radio Telescope (FAST). A combined analysis of the Zeeman measurements of quasar HI absorption, HI emission, OH emission, and HINSA reveals a coherent magnetic field from the atomic cold neutral medium (CNM) to the molecular envelope of the L1544. We find that the molecular envelope traced by HINSA is already magnetically supercritical, with a field strength comparable to that in the surrounding diffuse, magnetically subcritical CNM despite a large increase in density. The reduction of the magnetic flux relative to

*Email:chingtaochung@gmail.com, orcid.org/0000-0001-8516-2532

†Email:dili@nao.cas.cn, orcid.org/0000-0003-3010-7661

the mass, necessary for star formation, thus seems to happen during the transition from the diffuse CNM to the molecular gas traced by HINSA , earlier than envisioned in the classical picture where magnetically supercritical cores capable of collapsing into stars form out of magnetically subcritical envelopes[6,7]. The HINSA Zeeman effect opens up a new window on the interstellar magnetic field that is poised for rapid growth in the era of Square Kilometer Array and its precursors.

L1544 is a well-studied prototypical low-mass prestellar core [8] in the Taurus molecular cloud complex at a distance of about 140 pc [9]. The core has a mass of 3.2 solar mass ($M_\odot$) and a size of $\sim$ 0.1 pc [10], embedded in a 30 $M_\odot$ envelope with a flatten shape of 1 pc along the long axis [11] *. The core is characterized by a high central number density of $\sim 2 \times 10^6$ cm^{-3} [12], a low central temperature of $\sim$ 6 K [13], and strong depletion of carbon-bearing molecules [14]. Together with a slow infall velocity of $\sim$ 0.1 km s^{-1} and a narrow turbulent line width of 0.2 km s^{-1} [11,14,15], comprehensive chemical and dynamical modeling suggest that L1544 could be a quiescent core in an early transition between starless and protostellar phases [12,16,17].

We developed the so-called HINSA technique to reveal the atomic gas well mixed with molecular gas [4,5] and thus provide a rare probe of the transition from HI to H_2. The HINSA feature in L1544 has a strong absorption dip and a nearly thermalized narrow line width at a temperature lower than 15 K [4]. The non-thermal line width and centroid velocity of the HINSA are very close to those of the emission lines of OH, ^{13}CO, and C^{18}O molecules, and their column densities are

*In this paper, we refer to a core as an entity of dense molecular gas within a size of 0.1 pc, and an envelope as the molecular gas surrounding a core in a range of 0.1-1 pc.

essentially correlated [5]. The correlation of the line widths and column densities suggests that a significant fraction of the atomic hydrogen is located in the cold, well-shielded portions of L1544 and mixed with the molecular gas, distinguished from the broader absorption features seen in other surveys of HI throughout the Galaxy.

The previous Zeeman observations of OH emission line toward the L1544 center detect a magnetic field strength of 10.8 ± 1.7 μG with the Arecibo Telescope [18]. However, the OH Zeeman observations of the Green Bank Telescope (GBT) toward four locations of the envelope at a radius of 6.0' (0.24 pc) from the core center yield large uncertainties in the magnetic field strengths at the four locations, and a simultaneous fit for a single strength of all four locations yields a low-confident value of 2 ± 3 μG, leading to debates on whether the data can be used to constrain the structure of magnetic fields in the envelope because of limited quality [19–22]. Since the previous Zeeman observations cannot definitively determine the magnetic field strength in the envelope, sensitive observations of Zeeman effects of a new tracer are urgently needed. Unfortunately, Zeeman measurements in interstellar medium of non-masing sources are extremely sparse, and only the tracers of HI , OH, and CN have successfully produced systematic Zeeman measurements for reasons of abundance, Zeeman splitting Landé g-factor, and excitation conditions of the tracers [23]. Although the Zeeman effect of HI self-absorption feature have been found towards the directions of molecular clouds [24,25], the broad line widths of the absorption components are mostly associated with diffuse atomic gas rather than dense molecular gas. Considering that HI has a larger Landé g-factor than most molecules and is less affected by depletion at high densities than heavier molecules and that HINSA typically has a higher brightness temperature than most molecular

lines, it is natural to use HINSA to measure magnetic field strength in molecular gas.

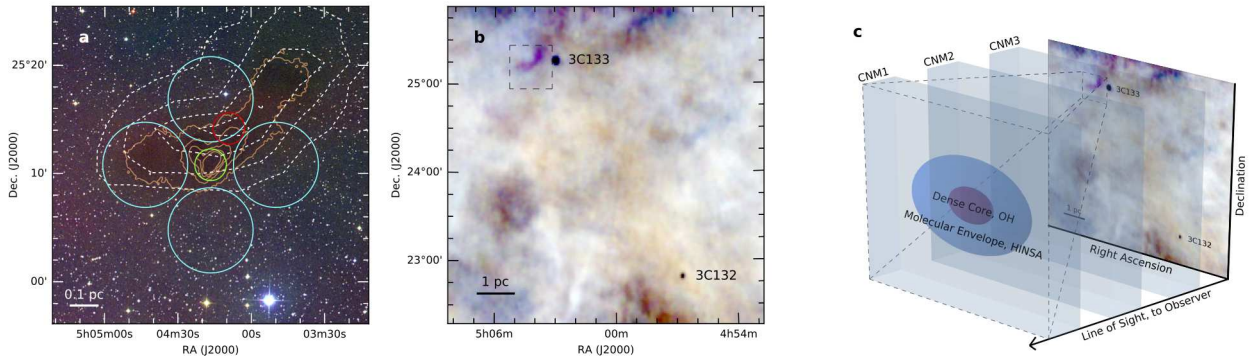

Figure 1: **L1544 core and illustration of the structure of interstellar medium from CNM to core. a,** a composite of DSS2 images of L1544 with *i*-band in red, *r*-band in green, and *b*-band in blue overlaid with HINSA and H_2 column density maps. White dashed contours are 30%, 50%, 70%, and 90% of the peak HINSA column density, and orange contours are 2, 4, 6, 8, 10×10^{21} cm^{-2} for the H_2 column density. The red, green, and cyan circles mark the locations and beam sizes of the FAST, Arecibo, and GBT Zeeman observations, respectively. **b,** a composite of three 0.5 km s^{-1} velocity slices of Arecibo GALFA-HI images at 6.2, 6.7, and 7.3 km s^{-1} LSR velocities in blue, green, and red. The dashed rectangle shows the region of **a**. The two absorption dots represent the locations of quasars 3C132 and 3C133. **c,** schematic view of CNMs, molecular envelope, and L1544 core.

We detected Zeeman splittings toward the HINSA column density peak at a distance of 3.6' (0.15 pc) away from the L1544 center (Fig. 1) at an angular resolution of 2.9' (0.12 pc) with FAST[26]. The spectra of the Stokes $I(v)$ and $V(v)$ parameters (where v denotes velocity) at 21-cm wavelength are shown in Fig. 2. The $I(v)$ spectrum contains HI emission of CNM and warm neutral medium (WNM) clouds in the direction toward the Taurus complex and a HINSA feature at

the centroid velocity of L1544. Least-squares fits of multiple gaussians with radiative transfer decompose the $I(v)$ into a foreground HINSA component, a background WNM component, and three CNM components between the HINSA and WNM. The fitted $I(v)$ profiles of the HINSA , CNM, and WNM components are shown in Fig. 2a. Our fitted parameters of the HINSA component are in good agreement with the previous HINSA observations [4,5], and our parameters of the CNM and WNM components are similar to the Arecibo results toward quasars around L1544 [27].

The $V(v)$ spectrum shows features of classic 'S curve' patterns proportional to the first derivatives of $I(v)$ for the HINSA , CNM, and WNM components, as expected for Zeeman splittings. The Zeeman splitting profile of HINSA has a maximum at high velocity and a minimum at low velocity, opposite to the Zeeman splitting profile of CNM1, the closest CNM component at a velocity similar to L1544, that shows positive V at low velocity and negative V at high velocity. From our least-squares fits to $V(v)$, we obtain the magnetic field strengths of the HINSA , CNM, and WNM components, listed in Table 2 of Methods. The fitted $V(v)$ profile of the HINSA and the total $V(v)$ profile of the five components are show in Fig. 2b, and the individual $V(v)$ profiles of the components are shown in Fig. 3. The HINSA Zeeman effect gives $B_{los} = 3.8 \pm 0.3$ μG, and the HI Zeeman effect of CNM1 gives $B_{los} = 4.0 \pm 1.1$ μG, where B_{los} is the magnetic field component projected along the line of sight with positive sign representing field pointing away from the observer. The magnetic field strengths of HINSA and CNM1 are consistent with the results of $B_{los} = 5.8 \pm 1.1$ μG and 4.2 ± 1.0 μG obtained from the Zeeman observations toward quasars 3C133 and 3C132, probing the magnetic fields of CNM1 at velocities of 8.0 ± 0.0 km s^{-1} and 8.1 ± 0.0 km s^{-1} at distances of 17.7' (0.72 pc) and 174.5' (7.1 pc) from L1544, respectively [28]. In addition, the weak strengths

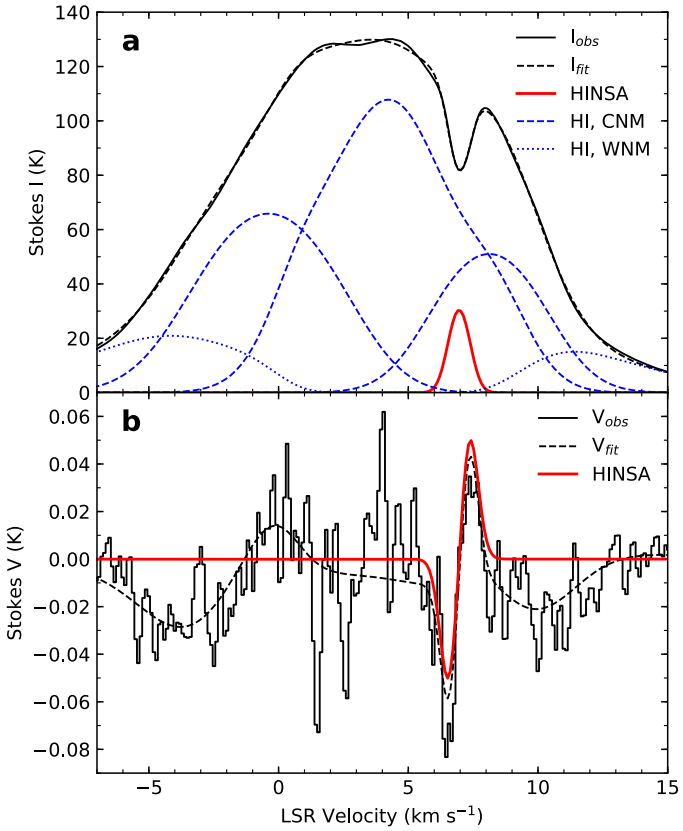

Figure 2: **The Stokes $I(v)$ and $V(v)$ spectra at 21-cm wavelength toward the HINSA column density peak.** **a**, The black profile represents the $I(v)$ spectrum. The red profile represents the absorption from the foreground HINSA component. The blue dashed and dotted profiles represent the emission of the CNM and WNM components, respectively. The CNM and WNM profiles include the absorption from the CNM components that lie in front but not include the absorption from HINSA . The black dashed profile represents the sum of the absorption and emission profiles. **b**, The black profile represents the $V(v)$ spectrum. The black dashed profile represents the sum of the Zeeman splitting profiles of the five components. The red profile represents the Zeeman splitting profile with B_{los} = 3.8 μG of the HINSA component.

inferred from Zeeman measurements are broadly consistent with the large dispersion of H-band polarization angles in the envelope of L1544 [29], given that near-infrared polarimetry traces the magnetic field component projected on the plane of sky and field strength is inversely proportional to the dispersion of polarization angles. For the second and third CNM components (CNM2 and CNM3) along the line of sight, our results of $B_{los,CNM2} = -7.6 \pm 1.0$ μG and $B_{los,CNM3} = 2.9 \pm 0.4$ μG are also consistent with the results of $B_{los,CNM2} = -9.6 \pm 6.3$ μG and $B_{los,CNM3} = -0.3 \pm 1.7$ μG toward quasar 3C133[28].

Comparing the Zeeman observations of HINSA , OH, and HI tracing the CNM1 and the molecular envelope of L1544, it is clear that the magnetic fields at distances of 0.15, 0.24, 0.72, and 7.1 pc from the center all have the same direction of B_{los} and consistent strengths roughly within the 1σ uncertainty in each measurement. Owning to the different excitation conditions and abundances of the three tracers, the HI absorptions toward 3C133 and 3C132 trace CNM with a kinematic temperature of about 100 K [28] and a number density of about 50 cm^{-3} [23], whereas the HINSA and OH observations trace the envelope of L1544 with a kinematic temperature of about 10–15 K [4] and a number density at the order of 10^3 cm^{-3} [5,23]. Despite the 1-2 orders of magnitude change in both temperature and density in the phase transition from the atomic CNM to the molecular envelope, the Zeeman observations reveal a magnetic field that is coherent in both direction and strength across multi-scales and multi-phases of the interstellar medium. Note that the magnetic field is also coherent in the line of sight, since the FAST results of HINSA and HI indicate consistent B_{los} at different depths of clouds along the line of sight. To constrain the uniformity of the coherent magnetic field, we performed a likelihood analysis with the assumption that the

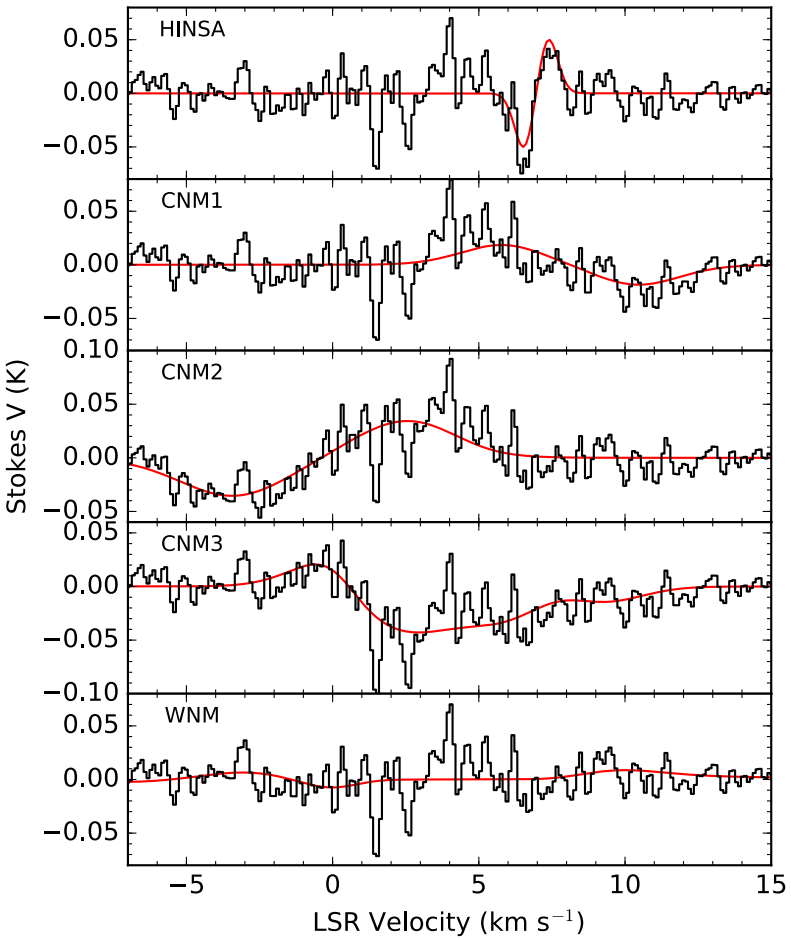

Figure 3: **The individual $V(v)$ profiles for the HINSA , CNM, and WMN components**. In each panel, the red profile represents the fitted Zeeman profile of the component, and the black profile represents the observed $V(v)$ subtracted by the fitted Zeeman profiles of the other four components. The CNM and WNM Zeeman profiles include the absorption from the CNM components that lie in front but not include the absorption from HINSA . The sum of the red profiles of the five components is the black dashed profile in Fig. 2b.

B_{los} of the coherent field follows a gaussian distribution with mean B_0 and intrinsic spread σ_0. Using the HINSA , OH, and HI Zeeman measurements, the maximum likelihood parameters are

$B_0 = 4.1 \pm 1.6\ \mu$G and $\sigma_0 = 1.2^{+1.2}_{-0.6}\ \mu$G, providing a better constraint of the field uniformity than the previous estimation of $B_0 = 4^{+10}_{-8}\ \mu$G by using only the OH results [21].

The Zeeman observations show that the magnetic fields from CNM to envelope are coherent and significantly weaker than the field in the core from the Arecibo OH Zeeman measurements. This finding is in agreement with the conclusion of comprehensive HI, OH, and CN Zeeman surveys, which suggest that the magnetic fields in HI clouds have a mediam value of 6 μG in total strength and do not scale vary significantly with density, whereas the magnetic fields in molecular clouds tend to increase with density above a critical number density of about 300 cm^{-3} [23]. The HINSA column densities of L1544 are correlated with those of ^{13}CO, which typically traces a number density of a few thousand cm^{-3}. Since the HINSA has a relatively weak magnetic field that has yet to increase beyond the values observed in the more diffuse gas, its density must be less than the critical density above which the field strength starts to increase with density. In other words, the HINSA observations suggest a critical density of at least a few thousand cm^{-3} in the L1544 system, which provides an important connection between the magnetic fields from HI clouds to molecular clouds that was not available before.

It is well known that the progenitor of molecular gas, the atomic CNM, is strongly magnetized, as measured by the dimensionless mass-to-magnetic flux ratio λ in units of the critical value of $2\pi G^{1/2}$ ($\lambda = 7.6 \times 10^{-21}[N/\mathrm{cm}^{-2}][B/\mu\mathrm{G}]^{-1}$ [1]), which is well below unity (i.e., magnetically subcritical) [30]. On the other hand, the immediate progenitors of stars, the prestellar cores of molecular clouds such as the L1554 core, are observed to be magnetically supercritical ($\lambda > 1$) [18],

which is required for the self-gravity to overwhelm the magnetic support and form stars through gravitational collapse. When and how the transition from the magnetically subcritical CNM that is incapable of forming stars through direct gravitational collapse to the supercritical star-forming cores is a central unresolved question in star formation.

Our HINSA Zeeman observations can be used to address this question. Using the physical parameters of the clouds (Table 1) and the statistically most probable value of the total field strength $B = 2B_{los}$, the λ of CNM1 is about 0.19–0.37, consistent with previous results [30]. The λ of the envelope and core of L1544 core is 2.5–3.5, which is well above unity, indicating that the transition to magnetic supercriticality has already occurred. Because the magnetic fields from CNM to envelope are coherent, the angles between the line of sight and B in the clouds should be similar. The relative values of λ between CNM1 and L1544 thus is considered to avoid the uncertainty in the geometrical correction from B_{los} to B [19]. Therefore, the molecular envelope of the L1544 core traced by HINSA is at least 6 times less magnetized relative to its mass (as measured by λ) compared to its ambient CNM. This is different from the classic theory of low-mass star formation, which envisions the transition from magnetic subcriticaliity to supercriticality occuring as the supercritical core forms out of the magnetically supported (subcritical) envelope [6,7]. Our results suggest that the transition to supercriticality occurs earlier, during the formation of the molecular envelope. In other words, by the time that the molecular envelope is formed, the problem of excessive magnetic flux as a fundamental obstacle to gravitational collapse and star formation is already resolved. The already magnetically supercritical envelope can in principle go on to form dense cores without having to reduce its magnetic flux relative to mass further, as

indicated by the comparable values of λ ($\sim$ 3) for both the molecular envelope and core of L1544 (see Table 1).

Table 1: **Physical Parameters of the Clouds**

Tracer/Cloud	B_{los} [μG]	N [10^{20} cm^{-2}]	λ
HI$_{3C132}$/CNM1	4.2 ± 1.0	4.05 ± 1.07 †	0.37 ± 0.13
HI$_{3C133}$/CNM1	5.8 ± 1.1	2.89 ± 1.03 †	0.19 ± 0.08
HINSA/envelope	3.8 ± 0.3	34.9 ± 0.1 ‡	3.5 ± 0.3
OH/core	10.8 ± 1.7	70.5 ± 0.2 ‡	2.5 ± 0.4

† Ref. 26.

‡ Obtained from the H_2 column density map in Fig. 1a.

In summary, the HINSA Zeeman observations reveal a coherent magnetic field from CNM to the envelope of a prestellar core, providing an important connection between the magnetic fields from HI clouds to molecular clouds. HINSA has features of strong absorption and narrow linewidth, making the Zeeman effect of HINSA prominent and relatively easy to identify. In addition, the detection rate of HINSA in dense cores and their molecular envelopes is high, and the foreground/background confusion in HINSA is minimized since the foreground gas usually has a small optical depth [4]. Therefore, HINSA has a great potential to become the fourth tracer to perform systematic Zeeman observations. Future HINSA Zeeman observations toward multiple locations of prestellar cores will reveal more details of magnetic field structures, offering guidance

on deciphering the role of magnetic fields in star formation.

1. McKee, C. F. & Ostriker, E. C. Theory of Star Formation. ARA&A **45**, 565–687 (2007). 0707.3514.

2. Hennebelle, P. & Inutsuka, S.-i. The role of magnetic field in molecular cloud formation and evolution. Frontiers in Astronomy and Space Sciences **6**, 5 (2019). 1902.00798.

3. Crutcher, R. M. & Kemball, A. J. Review of Zeeman Effect Observations of Regions of Star Formation K Zeeman Effect, Magnetic Fields, Star formation, Masers, Molecular clouds. Frontiers in Astronomy and Space Sciences **6**, 66 (2019). 1911.06210.

4. Li, D. & Goldsmith, P. F. H I Narrow Self-Absorption in Dark Clouds. ApJ **585**, 823–839 (2003). astro-ph/0206396.

5. Goldsmith, P. F. & Li, D. H I Narrow Self-Absorption in Dark Clouds: Correlations with Molecular Gas and Implications for Cloud Evolution and Star Formation. ApJ **622**, 938–958 (2005). astro-ph/0412427.

6. Shu, F. H., Adams, F. C. & Lizano, S. Star formation in molecular clouds: observation and theory. ARA&A **25**, 23–81 (1987).

7. Mouschovias, T. C. & Ciolek, G. E. Magnetic Fields and Star Formation: A Theory Reaching Adulthood. In Lada, C. J. & Kylafis, N. D. (eds.) The Origin of Stars and Planetary Systems, vol. 540 of NATO Advanced Study Institute (ASI) Series C, 305 (1999).

8. Snell, R. L. A study of nine interstellar dark clouds. ApJS **45**, 121–175 (1981).

9. Elias, J. H. A study of the Taurus dark cloud complex. ApJ **224**, 857–872 (1978).

10. Ward-Thompson, D., Motte, F. & Andre, P. The initial conditions of isolated star formation - III. Millimetre continuum mapping of pre-stellar cores. MNRAS **305**, 143–150 (1999).

11. Tafalla, M. et al. L1544: A Starless Dense Core with Extended Inward Motions. ApJ **504**, 900–914 (1998).

12. Aikawa, Y., Ohashi, N., Inutsuka, S.-i., Herbst, E. & Takakuwa, S. Molecular Evolution in Collapsing Prestellar Cores. ApJ **552**, 639–653 (2001). astro-ph/0202061.

13. Crapsi, A., Caselli, P., Walmsley, M. C. & Tafalla, M. Observing the gas temperature drop in the high-density nucleus of L 1544. A&A **470**, 221–230 (2007). 0705.0471.

14. Tafalla, M., Myers, P. C., Caselli, P., Walmsley, C. M. & Comito, C. Systematic Molecular Differentiation in Starless Cores. ApJ **569**, 815–835 (2002). astro-ph/0112487.

15. Caselli, P. et al. Molecular Ions in L1544. I. Kinematics. ApJ **565**, 331–343 (2002). astro-ph/0109021.

16. Li, Z.-Y., Shematovich, V. I., Wiebe, D. S. & Shustov, B. M. A Coupled Dynamical and Chemical Model of Starless Cores of Magnetized Molecular Clouds. I. Formulation and Initial Results. ApJ **569**, 792–802 (2002). astro-ph/0201019.

17. Keto, E., Caselli, P. & Rawlings, J. The dynamics of collapsing cores and star formation. MNRAS **446**, 3731–3740 (2015). 1410.5889.

18. Crutcher, R. M. & Troland, T. H. OH Zeeman Measurement of the Magnetic Field in the L1544 Core. ApJL **537**, L139–L142 (2000).

19. Crutcher, R. M., Hakobian, N. & Troland, T. H. Testing Magnetic Star Formation Theory. ApJ **692**, 844–855 (2009). 0807.2862.

20. Crutcher, R. M., Hakobian, N. & Troland, T. H. Self-consistent analysis of OH Zeeman observations. MNRAS **402**, L64–L66 (2010). 0912.3024.

21. Mouschovias, T. C. & Tassis, K. Testing molecular-cloud fragmentation theories: self-consistent analysis of OH Zeeman observations. MNRAS **400**, L15–L19 (2009). 0909.2031.

22. Mouschovias, T. C. & Tassis, K. Self-consistent analysis of OH-Zeeman observations: too much noise about noise. MNRAS **409**, 801–807 (2010). 1007.3741.

23. Crutcher, R. M., Wandelt, B., Heiles, C., Falgarone, E. & Troland, T. H. Magnetic Fields in Interstellar Clouds from Zeeman Observations: Inference of Total Field Strengths by Bayesian Analysis. ApJ **725**, 466–479 (2010).

24. Goodman, A. A. & Heiles, C. The Magnetic Field in the Ophiuchus Dark Cloud Complex. ApJ **424**, 208 (1994).

25. Heiles, C. A Holistic View of the Magnetic Field in the Eridanus/Orion Region. ApJS **111**, 245–288 (1997).

26. Li, D. et al. FAST in Space: Considerations for a Multibeam, Multipurpose Survey Using China's 500-m Aperture Spherical Radio Telescope (FAST). IEEE Microwave Magazine **19**, 112–119 (2018). 1802.03709.

27. Heiles, C. & Troland, T. H. The Millennium Arecibo 21 Centimeter Absorption-Line Survey. I. Techniques and Gaussian Fits. ApJS **145**, 329–354 (2003). astro-ph/0207104.

28. Heiles, C. & Troland, T. H. The Millennium Arecibo 21 Centimeter Absorption-Line Survey. III. Techniques for Spectral Polarization and Results for Stokes V. ApJS **151**, 271–297 (2004).

29. Clemens, D. P., Tassis, K. & Goldsmith, P. F. The Magnetic Field of L1544. I. Near-infrared Polarimetry and the Non-uniform Envelope. ApJ **833**, 176 (2016). 1610.05543.

30. Heiles, C. & Troland, T. H. The Millennium Arecibo 21 Centimeter Absorption-Line Survey. IV. Statistics of Magnetic Field, Column Density, and Turbulence. ApJ **624**, 773–793 (2005). astro-ph/0501482.

Acknowledgements This work is supported by the National Natural Science Foundation of China (NSFC) grant No. 11988101, U1931117, and 11725313; by CAS International Partnership Program No. 114A11KYSB20160008; and by the National Key R&D Program of China No. 2017YFA0402600. T.-C. C. is funded by Chinese Academy of Sciences Taiwan Young Talent Program. Grant No.2018TW2JB0002. T.-C. C. and J. T. are supported by Special Funding for Advanced Users, budgeted and administrated by Center for Astronomical Mega-Science (CAMS), Chinese Academy of Sciences. C. H. is funded by Chinese Academy of Sciences President's International Fellowship Initiative Grant No. 2020DM0005. Z.-Y. L. is supported in part by NASA 80NSSC20K0533 and NSF AST-1716259 and 1815784. This work made use of

data from FAST, a Chinese national mega-science facility built and operated by the National Astronomical Observatories, Chinese Academy of Sciences.

Author Contributions T.-C. C., D. L., and C. H. launched the FAST Zeeman project; T.-C. C. processed the data and analysis in consultation with C. H.; T.-C. C., Z.-Y. L., D. L., and C. H. drafted the paper; L. Q., Y. L. Y. , and J. T. made key contributions to arrange the FAST observations of L1544 and polarization calibration; S. H. J. provided the H_2 column density map.

Competing Interests The authors declare that they have no competing financial interests.

Methods

Data reduction The FAST Zeeman observations toward the HINSA column density peak in L1544 were carried out in 5 days in August, September, and November 2019 with a total integration time of 7.6 hours. The HINSA spectra were obtained with the central beam of the L-band 19-beam receiver [31]. The central beam has an average system temperature of 24 K, a main beam efficiency of 0.63, and a main beam diameter at the half-power point of 2.9' with a pointing accuracy of 7.9". The 19-beam receiver had orthogonal linear polarization feeds followed by a temperature stabilized noise injection system and low noise amplifiers to produce the X and Y signals of the two polarization paths. The XX, YY, XY, and YX correlations of the signals then were simultaneously recorded using the ROACH backend with 65536 spectral channels in each polarization. The spectral bandwidth was 32.75 MHz centered at the frequency of the HI 21-cm line for a channel spacing of 500 Hz, and the $V(v)$ spectrum presented in this work was Hanning-smoothed, which produced a spectral resolution of 0.21 km s^{-1}.

The data reduction including gain and phase calibrations of the two polarization paths, bandpass calibrations of the four correlated spectra, and polarization calibrations to generate Stokes I, Q, U, and V spectra was made with the IDL RHSTK package written by C. Heiles and T. Robishaw that is widely used for Arecibo and GBT polarization data. The 19-beam receiver is rotatable from -80° to +80° with respect to the line of equatorial latitude. The polarization calibrations used drifting scans of the continuum source 3C286 at rotation angles of -60°, -30°, 0°, 30°, and 60° over 1.5 hours surrounding its transit. The details of the polarization calibration procedure were provided in [32]. We performed polarization calibrations once a month during the observations. The

calibrated polarization of 3C286 of the three epochs were 8.9% ± 0.1%, 8.7% ± 0.2%, and 9.0% ± 0.1% for polarization degrees and 30.4° ± 0.3°, 33.8° ± 0.5°, and 29.4° ± 0.3° for polarization angles. Considering that the ionosphere can generate a faraday rotation of 1°–3° in polarization angle at L-band [33], our results were consistent with the intrinsic polarization degree of 9.5% and polarization angle of 33° of 3C286 at 1450 MHz [34]. In addition to the polarization observations of L1544 and 3C286, we observed the circularly polarized OH maser source IRAS02524+2046 [35] in order to verify that our procedures produced consistent B_{los}, including the sign or direction of the magnetic field, as had been obtained previously.

The convolutions of the sidelobes of the Stokes *V* beam with the spatial gradient of the Stokes *I* emission may generate a false 'S curve' in the *V* spectrum [28]. In order to check the credibility of our Zeeman detections, we measured the Stokes *V* beam of FAST and convolved the beam with the GALFA Stokes *I* cube [36] of L1544. The convolved *V* spectrum showed a profile with a shape similar to the *I* spectrum and a strength less than 0.03% of the *I* spectrum, different from the 'S curve' patterns in the observed *V* spectrum. Meanwhile, the 19-beam receiver was rotated to -45°, 0°, and 45° in the three epochs of the L1544 observations, and all of the three epochs showed 'S curve' patterns in the *V* spectra, indicating that our Zeeman results were true detections.

Multiple gaussians and radiative transfer fitting to $I(\mu)$ and $V(\mu)$ Our fitting of $I(v)$ adopts the equations of gaussian components and radiative transfer [27]. The expected profile of $I(v)$ consists of multiple CNM components providing opacity and also brightness temperature and a WNM

component providing only brightness temperature:

$$I(v) = I_{CNM}(v) + I_{WNM}(v). \tag{1}$$

The $I_{CNM}(v)$ is an assembly of N CNM components

$$I_{CNM}(v) = \sum_{n=1}^{N} I_{peak,n}(1 - e^{-\tau_n(v)})e^{-(\sum_{m=1}^{M}\tau_m(v)+\tau_0)}, \tag{2}$$

where the subscript m with its associated optical depth profile $\tau_m(v)$ represents each of the M CNM clouds that lie in front of cloud n. The optical depth of the ith component is

$$\tau_i(v) = \tau_i e^{-[(v-v_{0,i})/\sigma_{v,i}]^2} \tag{3}$$

in which τ_0 represents the HINSA providing only opacity and no brightness temperature. For the WNM in the background,

$$I_{WNM}(v) = I_{peak,WNM}e^{-[(v-v_{0,WNM})/\sigma_{v,WNM}]^2}e^{-\sum_{i=0}^{N}\tau_i(v)}. \tag{4}$$

The fitting of $I(v)$ thus yields values for I_{peak}, τ, v_0, and σ_v of the components.

We consider the radiative transfer of $V(v)$ in terms of right circular polarization (RCP) and left circular polarization (LCP). The Zeeman effect states that with the existence of B_{los}, the frequency of RCP shifts from its original frequency ν_0 to $\nu_0 + \nu_z$ and the frequency of LCP shifts to $\nu_0 - \nu_z$ with $\nu_z = (Z/2) \times B_{los}$, where Z is the Zeeman splitting factor (2.8 Hz μG^{-1} for HI 21-cm line). Since the RCP and LCP are orthogonal components of radiation, the radiative transfer processes of RCP and LCP are independent to each other. For RCP, Equation (1) becomes

$$T_{RCP} = T_{RCP,CNM}(v, \tau_{RCP,i}) + T_{RCP,WNM}(v, \tau_{RCP,i}), \tag{5}$$

where for the ith component, $T_{RCP,i} = I_{peak,i}/2$, $\tau_{RCP,i}$ is optical depth in the RCP radiation to substitute the τ_i in Equation (3) with $\tau_{RCP,i} = \tau_i(v_0 + v_{z,i})$ for $B_{los,i}$ of the component, and the parameters of v_0 and σ_v keep the same. Similarly, for LCP,

$$T_{LCP} = T_{LCP,CNM}(v, \tau_{LCP,i}) + T_{LCP,WNM}(v, \tau_{LCP,i}) \tag{6}$$

with $T_{LCP,i} = I_{peak,i}/2$ and $\tau_{LCP,i} = \tau_i(v_0 - v_{z,i})$. The fitting of $V(v) = T_{RCP} - T_{LCP} + cI(v)$, which includes a c term accounting for leakage of $I(v)$ into $V(v)$, thus yields values for B_{los} of the components. In Table 2, we list the parameters of the components obtained from least-squares fits to $I(v)$ and $V(v)$. The leakage of our HINSA Zeeman observations is $c = 0.034\%$.

Table 2: **Gaussian Fit Parameters**

Component	I_{peak} [K][a]	τ [b]	v_{LSR} [km s^{-1}] [c]	σ_v [km s^{-1}] [d]	B_{los} [μG]	Order [e]
HINSA	–	0.32 ± 0.01	6.97 ± 0.01	0.40 ± 0.01	3.8 ± 0.3	0
CNM1	90.34 ± 5.49	0.83 ± 0.12	8.12 ± 0.11	1.86 ± 0.05	4.0 ± 1.1	1
CNM2	116.33 ± 1.78	0.84 ± 0.08	-0.39 ± 0.33	2.41 ± 0.13	-7.6 ± 1.0	2
CNM3	135.31 ± 2.04	10.45 ± 0.95	4.38 ± 0.09	2.04 ± 0.06	2.9 ± 0.4	3
WNM	46.70 ± 2.47	–	2.63 ± 0.04	6.44 ± 0.09	3.0 ± 1.7	4

[a] I_{peak} is the intrinsic peak Stokes I emission. We do not fit I_{peak} for HINSA because it is an absorption component.

[b] τ is the central opacity. We do not fit τ for WNM because it is a background component.

[c] v_{LSR} is the central LSR velocity.

[d] σ_v is the gaussian dispersion.

[e] The order of the component along the line of sight. Order begins with 0, and increasing numbers mean increasing

distance along the line of sight.

HiNSA and H_2 column density maps We show the HiNSA and H_2 column density maps of L1544 in Fig. 1a, and we use the H_2 column density map to calculate the N at the beams of FAST and Arecibo observations in Table 1. The HiNSA column density map is a revision of the Fig. 8 in ref. 14. To derive the H_2 column density map, we retrieved the level 2.5 processed, archival Herschel images that were taken at 250/350/500 μm using the SPIRE instrument [37], (obsID: 1342204842). We smoothed the Herschel images to a common angular resolution of the 36" beam at 500 μm and regridded the images to the same pixel size of 6". We performed least-squares fits of the 250/350/500 μm spectral energy distributions weighted by the squares of the measured noise levels to derive the pixel-to-pixel distributions of dust temperature T_d and dust optical depth τ_ν using $S_\nu = \Omega_m B_\mu(T_d)(1 - e^{-\tau_\nu})$, where S_ν is the flux density at frequency ν, Ω_m is the is the solid angle of the pixel, $B_\mu(T_d)$ is the Planck function at T_d, and $\tau_\nu = \tau_{230}(\nu[GHz]/230)^\beta$ with dust opacity index β of 1.8. Next, we obtained the H_2 column density with $N = g\tau_{230}/(\kappa_{230}\mu_m m_H)$, where $g = 100$ is the gas-to-dust mass ratio, $\kappa_{230} = 0.09$ cm^2 g^{-2} [38] is the dust opacity at 230 GHz, $\mu_m = 2.8$ is the the mean molecular weight, and m_H is the atomic mass of hydrogen. To estimate the uncertainties in the H_2 column density, we used a Monte-Carlo technique. For each pixel, we created artificial 250/350/500 μm flux densities by adding the original flux densities with normal-distributed errors taking account the uncertainty in the measured flux and a 10% correlation for the calibration uncertainty in SPIRE [39]. We then estimated the uncertainty in each pixel with 1000 fittings of the H_2 column density. The N and its uncertainty in Table 1 were obtained from the convolutions of the H_2 column density map and uncertainty map with the FAST and Arecibo

beams.

Maximum likelihood We adopt the analysis of maximum likelihood [21] to study the uniformity of magnetic fields in the envelope of L1544. Assuming that the true B_{los} follows a gaussian distribution with mean B_0 and intrinsic spread σ_0, the likelihood l_j for a single observation to measure B_j with gaussian error σ_j is proportional to the convolution of the probability $\exp[-(B - B_0)^2/2\sigma_0^2]/\sqrt{2\pi}\sigma_0$ for the magnetic field to have a true value of B with the probability $\exp[-(B - B_j)^2/2\sigma_j^2]/\sqrt{2\pi}\sigma_j$ of observing a value B_j of the field. Therefore, l_j is the integral over all possible true values of the magnetic field

$$l_j = \int_{-\infty}^{\infty} \mathrm{d}B \frac{\exp[-(B - B_j)^2/2\sigma_j^2]}{\sqrt{2\pi}\sigma_j} \frac{\exp[-(B - B_0)^2/2\sigma_0^2]}{\sqrt{2\pi}\sigma_0}. \quad (7)$$

While the overall likelihood $\mathcal{L}$ for a set of observations is the product of individual likelihoods of the observations ($\mathcal{L} = \prod_{J=1}^{N} l_j$), the B_0 and σ_0 can be estimated by maximizing the likelihood $\mathcal{L}$. After performing the integration in Equation (7) and some algebraic manipulations,

$$\mathcal{L}(B_0, \sigma_0) = \left(\prod_{J=1}^{N} \frac{1}{\sqrt{\sigma_0^2 + \sigma_j^2}} \right) \exp\left[-\frac{1}{2} \sum_{j=1}^{N} \frac{(B_j - B_0)^2}{\sigma_0^2 + \sigma_j^2} \right]. \quad (8)$$

Fig. 4 shows the distribution of $\mathcal{L}$ as functions of B_0 and σ_0 and the probability distributions of B_0 and σ_0 by integrating $\mathcal{L}$ along the B_0 axis and the σ_0 axis, respectively. The probability distribution of B_0 is similar to a normal distribution with a mean value of 4.1 μG and a standard deviation of 1.6 μG. The probability distribution of σ_0 is highly asymmetric since the values of σ_0 cannot be negative. The first, second, and third quartiles of the σ_0 distribution are 0.6, 1.2, and 2.4 μG. We therefore suspect that the Zeeman measurements in the L1544 envelope can be explain by

a magnetic field with $B_0 = 4.1 \pm 1.6\,\mu$G and $\sigma_0 = 1.2^{+1.2}_{-0.6}\,\mu$G.

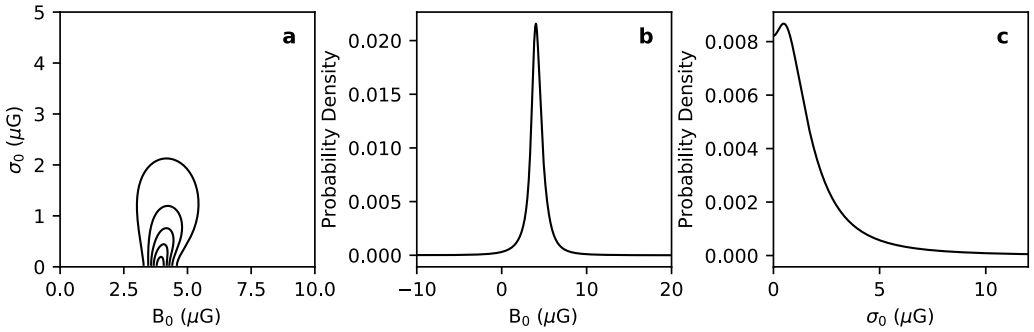

Figure 4: Likelihood $\mathcal{L}$ for the coherent magnetic field to have mean (B_0) and spread (σ_0) values. **a**, contours of $\mathcal{L}$ as functions of B_0 and σ_0 plotted at 10%, 30%, 50%, 70%, and 90% of the peak value. **b**, the probability distribution of B_0 while allowing all possible values of σ_0. **c**, the probability distribution of σ_0 while allowing all possible values of B_0.

Data availability FAST raw data are available from the http://fast.bao.ac.cn site one year after data-taking, per data policy of FAST. Due to the large data volume of this work and the speciality of polarization calibration, interested users are encouraged to contact the corresponding author to arrange data transfer. The reduced $I(v)$ and $V(v)$ spectra are available at https://github.com/taochung/HINSAzeeman.

Code availability The codes analyzing the $I(v)$ and $V(v)$ spectra reported here are available at https://github.com/taochung/HINSAzeeman. The IDL RHSTK package is available at http://w.astro.berkeley.edu/ heiles/.

31. Jiang, P., and 20 colleagues The fundamental performance of FAST with 19-beam receiver at L band. Research in Astronomy and Astrophysics. 20, (2020).

361 32. Heiles, C., and 9 colleagues Mueller Matrix Parameters for Radio Telescopes and Their Ob-
362 servational Determination. PASP. 113, 1274-1288 (2001).

363 33. Jehle, M., M. Ruegg, L. Zuberbuhler, D. Small, and E. Meier Measurement of Ionospheric
364 Faraday Rotation in Simulated and Real Spaceborne SAR Data. IEEE Transactions on Geo-
365 science and Remote Sensing. 47, 1512-1523 (2009).

366 34. Perley, R. A. and B. J. Butler Integrated Polarization Properties of 3C48, 3C138, 3C147, and
367 3C286. ApJS. 206, (2013).

368 35. McBride, J. and Heiles, C. An Arecibo Survey for Zeeman Splitting in OH Megamaser Galax-
369 ies. ApJ. 763, (2013).

370 36. Peek, J. E. G. The Galactic Arecibo L-Band Feed Array Data Release 2: Pipelines and Visu-
371 alizations. Astronomical Data Analysis Software and Systems XXV. 512, 411 (2017).

372 37. Griffin, M. J., Abergel, A., Abreu, A., et al. 2010, A&A, 518, L3. doi:10.1051/0004-
373 6361/201014519

374 38. Ossenkopf, V. & Henning, T. 1994, A&A, 291, 943

375 39. Roy, A., André, P., Palmeirim, P., et al. 2014, A&A, 562, A138. doi:10.1051/0004-
376 6361/201322236

Figures

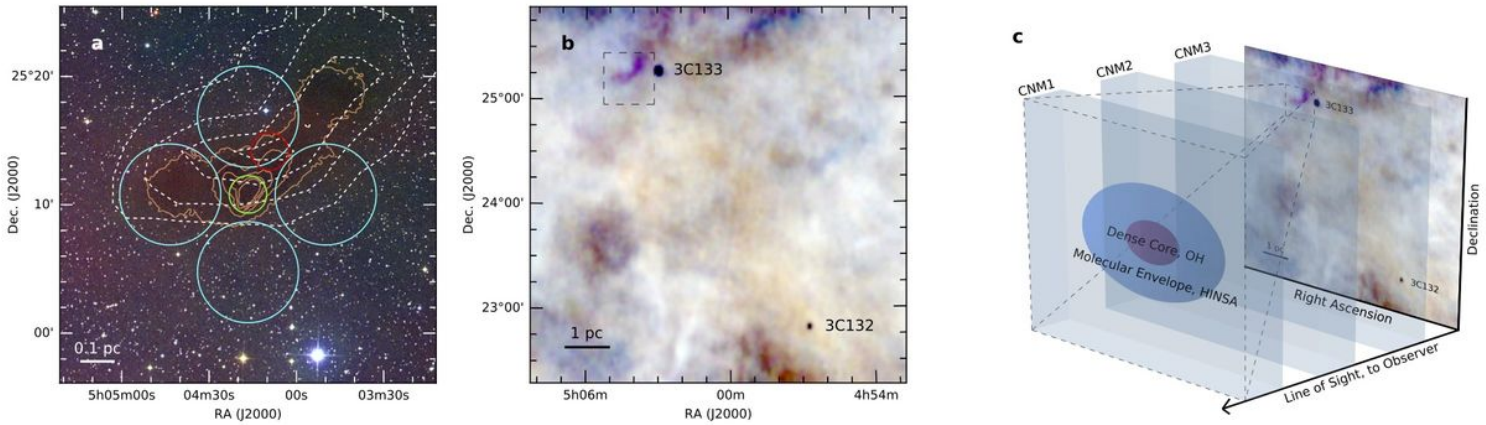

Figure 1

L1544 core and illustration of the structure of interstellar medium from CNM to core (see Manuscript file for full figure legend)

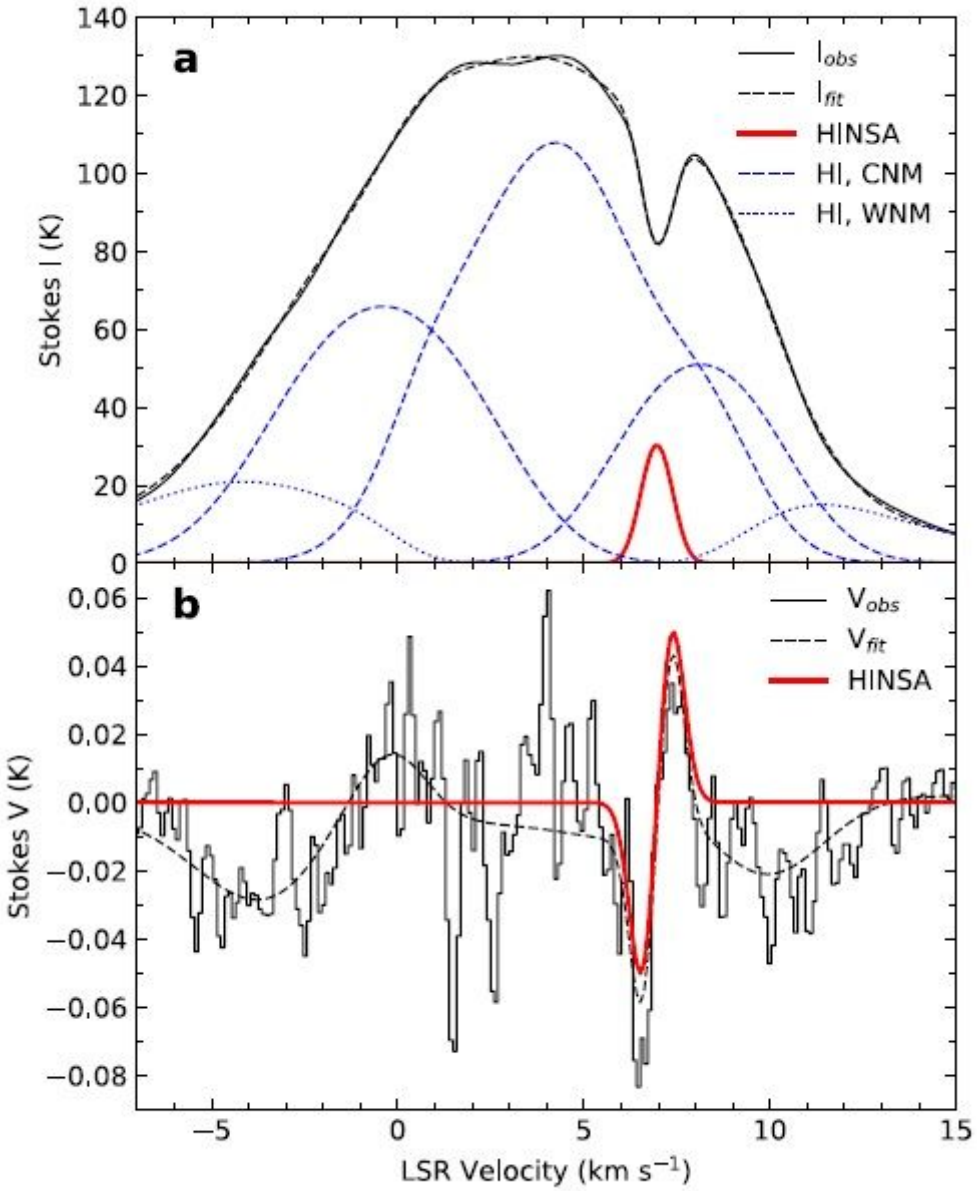

Figure 2

The Stokes I(v) and V(v) spectra at 21-cm wavelength toward the HINSA column density peak. (see Manuscript file for full figure legend)

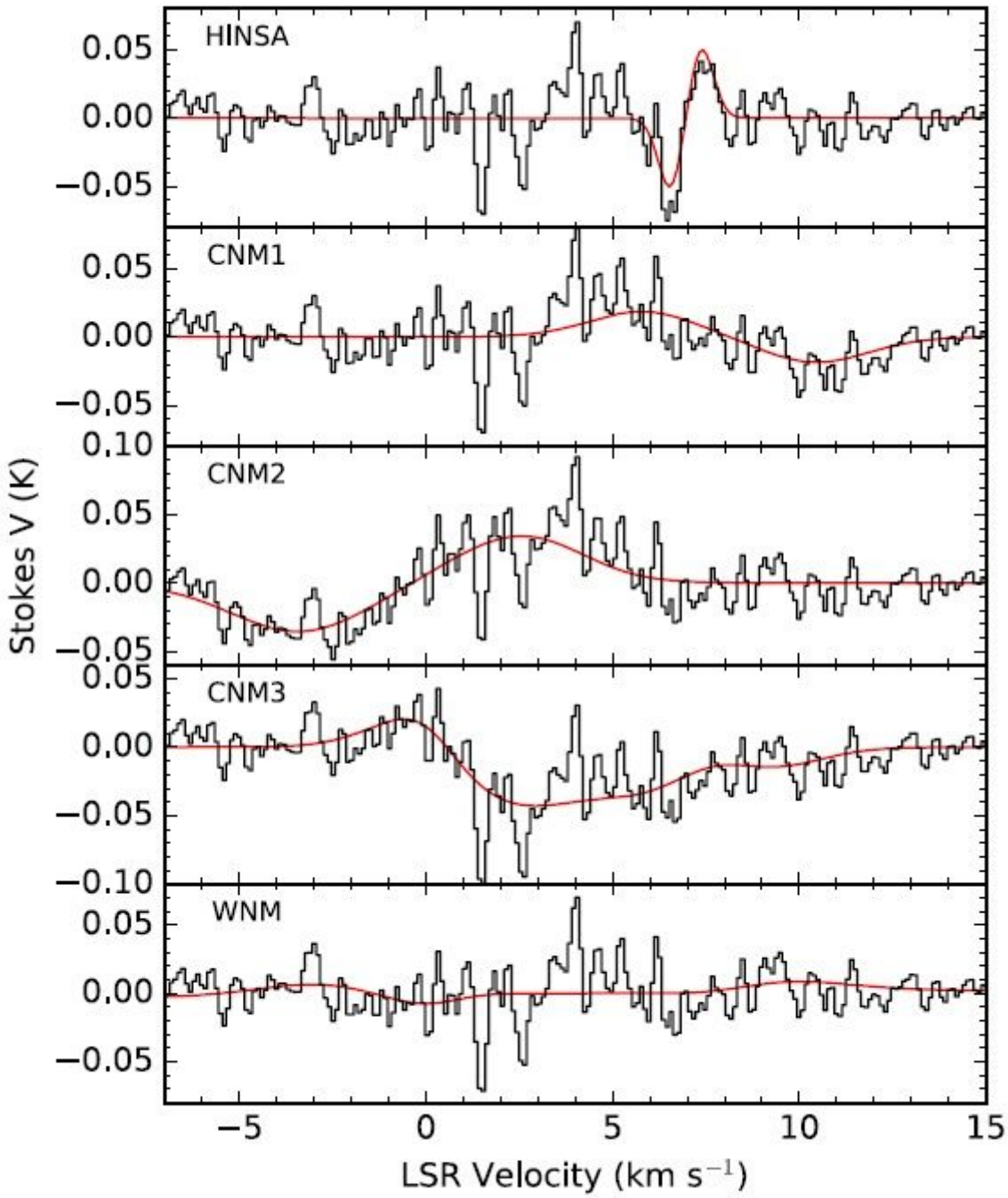

Figure 3

The individual V(v) profiles for the HINSA , CNM, and WMN components. (see Manuscript file for full figure legend)

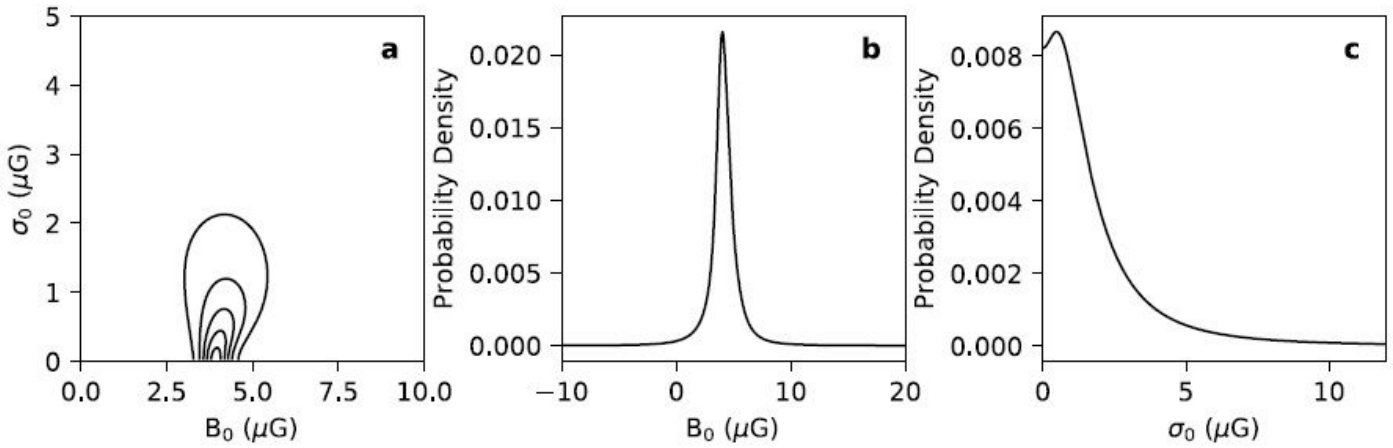

Figure 4

Likelihood L for the coherent magnetic field to have mean (B0) and spread (o0) values. (see Manuscript file for full figure legend)